VIP Antitumor Agents Very Important Paper

International Edition: DOI: 10.1002/anie.201510031
German Edition: DOI: 10.1002/ange.201510031

Synthesis of Iron Nanometallic Glasses and Their Application in Cancer Therapy by a Localized Fenton Reaction

Chen Zhang, Wenbo Bu, Dalong Ni, Shenjian Zhang, Qing Li, Zhenwei Yao, Jiawen Zhang, Heliang Yao, Zheng Wang, and Jianlin Shi**

Abstract: *Metallic glasses and cancer theranostics are emerging fields that do not seem to be related to each other. Herein, we report the facile synthesis of amorphous iron nanoparticles (AFeNPs) and their superior physicochemical properties compared to their crystalline counterpart, iron nanocrystals (FeNCs). The AFeNPs can be used for cancer theranostics by inducing a Fenton reaction in the tumor by taking advantage of the mild acidity and the overproduced H_2O_2 in a tumor microenvironment: Ionization of the AFeNPs enables on-demand ferrous ion release in the tumor, and subsequent H_2O_2 disproportionation leads to efficient $^{\bullet}OH$ generation. The endogenous stimuli-responsive $^{\bullet}OH$ generation in the presence AFeNPs enables a highly specific cancer therapy without the need for external energy input.*

Since their inception in 1960,[1] amorphous metals and alloys, which can also be described as metallic glasses (MGs) with a disordered atomic structure, have attracted great attention owing to their extraordinary properties. However, despite the promising prospects of bulk metallic glasses (BMGs) for various structural applications,[2] the mysterious nanometallic glasses (NMGs), which display novel electromagnetic properties and are rather reactive,[3] have received very little attention. The key bottleneck is the need for very particular synthesis conditions, such as the very high cooling rate (usually higher than $10^6\,K\,s^{-1}$) that is required to freeze the molten metal while suppressing the nucleation of crystalline phases.[4]

Cancer therapy by designing agents that are responsive to the tumor microenvironment is another emerging field. The acidic nature (pH 6.5–6.9) of solid tumors has been exploited by the development of many drug release systems (DRSs) where drug release is triggered by low pH values.[5] On the other hand, cancer cells and tissues produce large amounts of hydrogen peroxide, which is obtained from mitochondria-generated superoxide ions in a process that is catalyzed by the overexpressed superoxide dismutase (SOD).[6] The accumulation of H_2O_2 in cancer cells has thus been exploited as a spontaneous trigger for chemotherapy by responsive drug release,[7] or as an endogenous O_2 producer for enhanced photodynamic therapy (PDT).[8] From an electrochemical standpoint, the energy contained in H_2O_2 (standard reduction potential $E_{(H_2O_2/H_2O)} = 1.78$ V) is between that of PDT-related reactive oxygen species (ROS, mainly the hydroxyl radical ($E_{(^{\bullet}OH/H_2O)} = 2.80$ V) and singlet oxygen ($E_{(^1O_2/H_2O)} = 2.17$ V)) and O_2 ($E_{(O_2/H_2O)} = 1.23$ V). As this H_2O_2 energy utilization process is rather circuitous and requires laser excitation, the development of direct energy conversion strategies that do not require external energy input is highly desired, because these methods may benefit from enhanced therapeutic specificity and treatment simplicity.

The prodrug, namely the ferrous ion, enables the disproportionation of H_2O_2 to efficiently generate $^{\bullet}OH$ radicals[9] in the Fenton reaction, which was developed a long time ago, but has remained highly attractive. Chemodynamic therapy (CDT) can thus be achieved by using endogenous chemical energy to produce ROS, which induce cell death, without the need for external energy input by laser irradiation, thus circumventing the limitations posed by the penetration of light through tissues. In this regard, the anticancer activity of ferrocene and its derivatives, which was described in several pilot studies, has demonstrated preliminary feasibility.[10] However, owing to the non-specificity during circulation in the blood stream, these molecular Fe^{II} carriers may suffer from premature bio-oxidation processes, which result from the relatively low potential of the Fe^{3+}/Fe^{2+} redox couple (0.77 V), and even cause serious side effects in noncancerous regions with H_2O_2 overproduction that is the result of lipopolysaccharide-induced inflammation, for example.[11]

Considering the reactive nature of MGs, which is due to the metastable random structure that is devoid of long-range order, we decided to synthesize amorphous Fe^0 nanoparticles (AFeNPs), which are expected to be rapidly ionized in acidic tumors for on-demand Fe^{II} release and enable a subsequent localized Fenton reaction for specific cancer therapy. Owing to the stimuli-responsive nature of this process, the therapy can be highly specific.

The AFeNPs were synthesized according to a novel synthetic strategy in aqueous bubbles (hubble-bubble approach) to avoid the traditionally employed harsh condi-

[*] Dr. C. Zhang, Prof. W. Bu, Dr. D. Ni, Dr. Q. Li, Dr. H. Yao, Prof. Z. Wang, Prof. J. Shi
State Key Laboratory of High Performance Ceramics and Superfine Microstructure, Shanghai Institute of Ceramics
Chinese Academy of Sciences
1295 Ding-xi Road, Shanghai 200050 (P. R. China)
E-mail: wbbu@mail.sic.ac.cn
jlshi@mail.sic.ac.cn
Dr. S. Zhang
Department of Radiology, Shanghai Cancer Hospital
Fudan University
270 Dong-an Road, Shanghai 200032 (P. R. China)
Prof. Z. Yao, Prof. J. Zhang
Department of Radiology, Huashan Hospital
Fudan University
12 Urumqizhong Road, Shanghai 200040 (P. R. China)

Supporting information for this article is available on the WWW under http://dx.doi.org/10.1002/anie.201510031.

tions. In brief, the reduction of Fe^{3+} was designed to occur in the bubble films constructed by the amphiphilic block copolymer F-127 (Figure 1a,b; see also the Supporting Information, Figure S1). As the precursor solution is

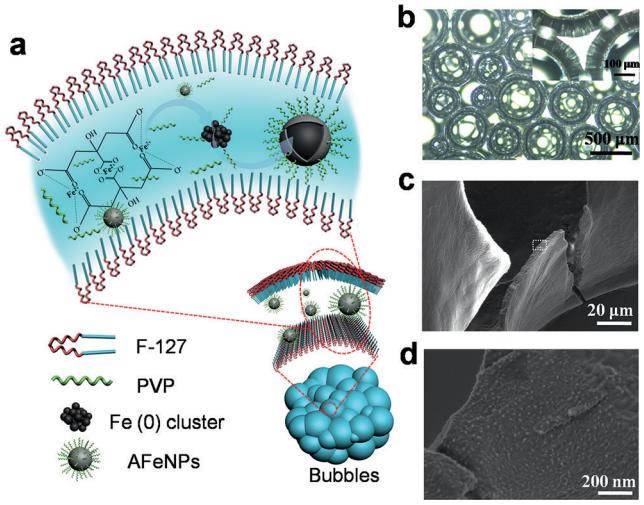

Figure 1. a) Preparation of AFeNPs. b) Microscopic image of the bubbles generated by the hubble-bubble process. Inset: enlarged image. c) SEM bright-field image of fragments of a bubble film supported by solid PVP and F-127 after freeze-drying under vacuum. d) SEM/BSE image of the indicated region (dashed rectangle) in (c).

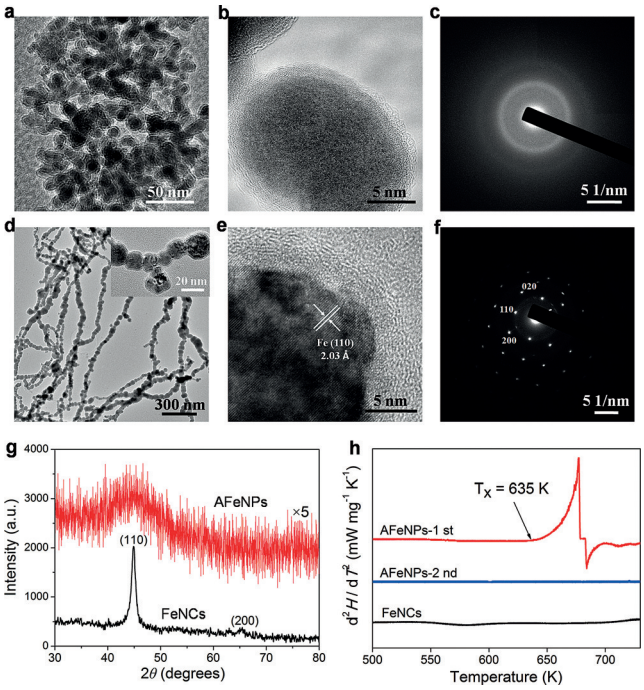

Figure 2. Low- and high-resolution TEM images of AFeNPs (a,b) and FeNCs (d,e), and their corresponding SAED patterns (c and f, respectively). The inset in (d) is an enlarged image. g) XRD patterns of the AFeNPs (×5) and FeNCs. h) Comparison of the derivative DSC traces of the FeNCs and AFeNPs (first measurement: red line, second measurement: blue line).

restricted to the small space between the F-127 bilayers, the long-range diffusion of iron atoms is effectively hindered, and nucleation and the growth of crystalline phases are thus suppressed. The further suppression of nucleation and growth was also achieved by substantially increasing the viscosity by the addition of PVP, and decreasing the concentration of free iron ions by the addition of citrate as a chelator (Figure S2b). Fragments of the freeze-dried bubble film (Figure 1c) thus generated were analyzed by scanning electron microscopy (SEM). The backscattered electron (BSE) image shows a clear *Z*-contrast, revealing the presence of well-dispersed nanoparticles with high *Z* values in the organic phase (Figure 1d), which is where the AFeNPs are synthesized in the bubble films. Very importantly, this hubble-bubble synthetic procedure turned out to be widely applicable as amorphous Co and Ni nanoparticles could be obtained under similar hubble-bubble conditions (Figure S3, Table S1).

To evaluate the amorphous structure of the AFeNPs, Fe^0 nanocrystals (FeNCs) were prepared for comparison. A transmission electron microscope (TEM) image of the as-synthesized AFeNPs shows their overall morphology (Figure 2a) and reveals their high uniformity with diameters of about 10–20 nm. The absence of lattice fringes in the high-resolution TEM (HRTEM) image (Figure 2b) indicates their amorphous nature, which was further confirmed by the characteristic diffuse halo in the selected area electron diffraction (SAED) pattern (Figure 2c). In contrast, the FeNCs synthesized in the absence of bubbles induced by F-127 are well-crystallized, which was confirmed by their clearly defined lattice fringes and a series of distinct diffraction spots corresponding to a body-centered cubic (bcc) iron framework (Figure 2e,f). The glassy nature of the AFeNPs was further confirmed by their significantly broadened X-ray diffraction (XRD) peak (Figure 2g) and the typical unidirectional crystallization transition (Figure S4) that was determined by derivative differential scanning calorimetry (DSC; Figure 2h). In both the AFeNPs and FeNCs, the 2 nm thick shell consists of PVP and iron oxide or hydroxide ($FeO_x(OH)_y$; Figure S5) and effectively protects the metastable Fe^0 inner core from oxidation.

Interestingly, the AFeNPs present several unique physicochemical properties compared with the FeNCs. Their specific saturation magnetization is 25% higher than that of the FeNCs (Figure 3a), with a soft magnetic characteristic featuring a slender hysteresis loop (Figure 3b,c). Furthermore, the ferromagnetic resonance (FMR) spectrum of the FeNCs contained a clear, asymmetric FMR signal split at approximately $g = 2.0$, suggesting that the FeNCs display remarkable magnetocrystalline anisotropy (Figure 3d). The AFeNPs, on the other hand, are devoid of magnetocrystalline anisotropy, which arises from an ordered atomic arrangement, as the energy barriers impeding the migration of magnetic domain walls and the reversal of magnetization are negligible,[12] rendering the AFeNPs more sensitive to the applied magnetic field.[13]

Surprisingly, despite the similarities in their TEM particle size, surface modification, and zeta potential (Figure S6), the AFeNPs are significantly more dispersible than the FeNCs

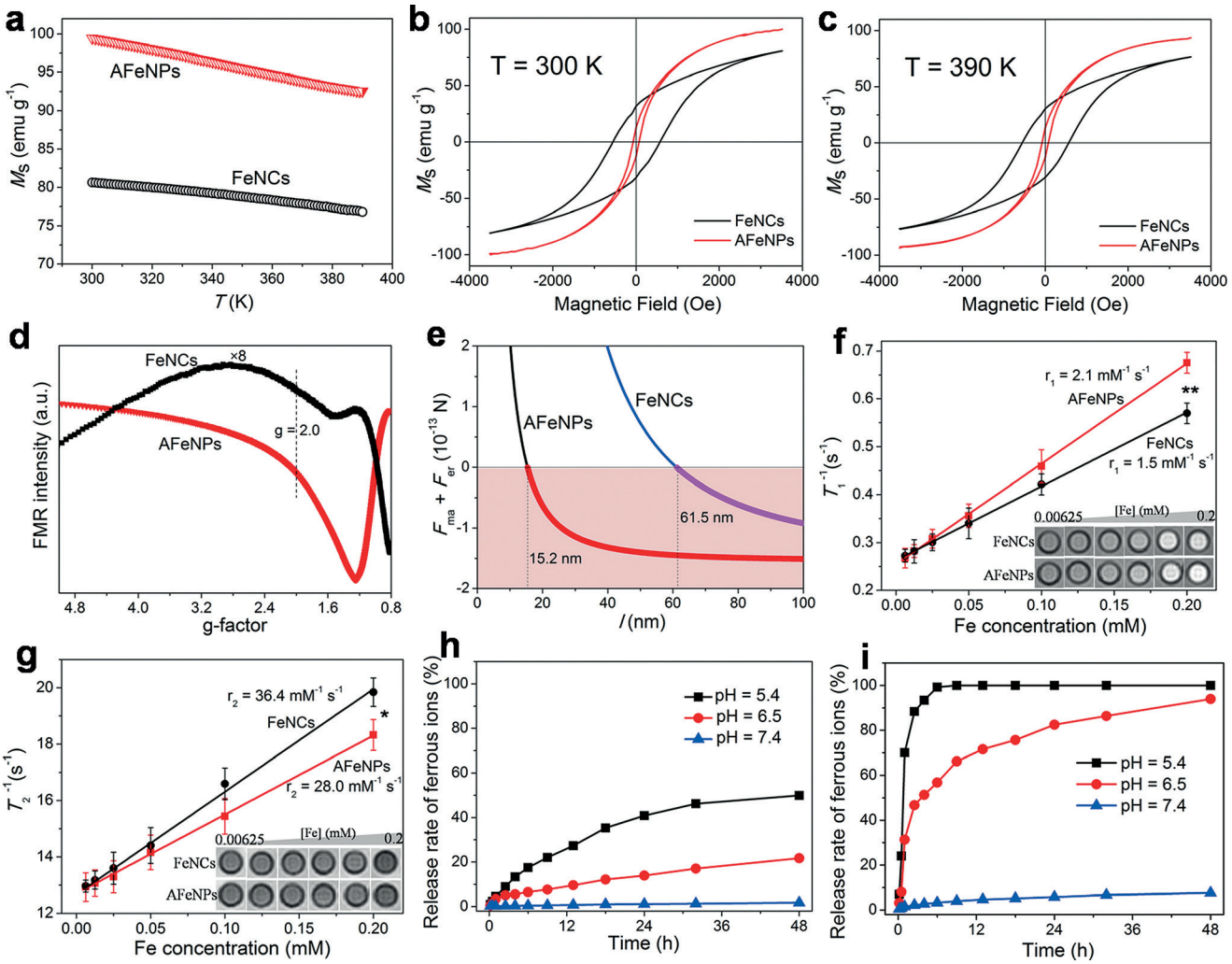

Figure 3. a) Temperature-dependent magnetization of the FeNCs and AFeNPs and the corresponding magnetic hysteresis loops at $T = 300$ K (b) and $T = 390$ K (c). d) FMR spectra of FeNCs and AFeNPs obtained at room temperature. e) Calculated distance-dependent forces resulting from magnetic attraction (F_{ma}, positive) and electrostatic repulsion (F_{er}, negative) in dispersed FeNC and AFeNP systems. g, h) The longitudinal (T_1^{-1}) and transverse relaxation rates (T_2^{-1}), respectively, of the FeNCs and AFeNPs measured at 3.0 T. Inset: Corresponding MR images of samples with various Fe concentrations ($n = 3$, mean ± s.d., $*P < 0.05$, and $**P < 0.01$). h, i) Time-dependent ionization of FeNCs and AFeNPs, respectively, at various pH values.

(Figures S7 and S8). To understand this discrepancy, the critical aggregation distance was analyzed by calculations (Figure 3e; see also Figure S9). The critical aggregation distance of the AFeNPs (15.2 nm) is about one fourth of that of the FeNCs (61.5 nm), and a little smaller than their TEM size (ca. 16 nm), implying that there always is a repulsive force between AFeNPs with diameters greater than 15.2 nm. Conversely, an attractive force will inevitably induce the aggregation of FeNCs when they are closer than their critical aggregation distance. The superior dispersibility of the AFeNPs is due to the decreased magnetic attraction between these particles, which can essentially be attributed to weak remanent magnetic induction because of their amorphous nature.

We next examined the relaxation properties of the FeNCs and AFeNPs to determine whether they could serve as contrast agents for magnetic resonance imaging (MRI). Meaningfully, a clear, positive signal (T_1-weighted MRI) enhancement was observed for both FeNCs and AFeNPs (Figure 3f), which may result in a higher visual contrast sensitivity compared to T_2-weighted MRI from a clinical point of view. The AFeNPs display a relatively high longitudinal relaxivity ($r_1 = 2.1$ mM^{-1}s^{-1}) and a low transverse relaxivity ($r_2 = 28.0$ mM^{-1}s^{-1}; Figure 3g), leading to a smaller r_2/r_1 ratio (13.3) than for the FeNCs ($r_2/r_1 = 24.3$), which suggests that the AFeNPs are a more efficient T_1 contrast agent. The higher r_1 observed for the AFeNPs is believed to arise from the intrinsic spin canting effect induced by the chaotic arrangement of iron atoms, which should effectively perturb the spin–lattice relaxation process of the protons.[14] Meanwhile, the higher B_r value arising from the magnetocrystalline anisotropy of FeNCs may induce a stronger local magnetic-field inhomogeneity for the water protons nearby during the dephasing process, leading to accelerated spin–spin relaxation and subsequently a slightly enhanced transverse relaxivity than for the AFeNPs.[15]

Finally, we compared the release of ferrous ions from the FeNCs and AFeNPs at various pH values. Ideally, a perfect carrier should release its cargo at once when it is transferred from neutral to mildly acidic conditions, such as those in the tumor microenvironment. A clear pH-dependent ionization and reluctant release of ferrous ions at neutral pH were observed for both FeNCs and AFeNPs (Figure 3h,i). The release rate of ferrous ions from the AFeNPs reached 57% at pH 6.5 and 100% at pH 5.4 within six hours, which is much higher than that from the FeNCs owing to their metastable random structure. The time dependence of the MR signal intensity further confirmed the on/off nature of the ferrous ion release and indicated that the AFeNPs are much more ionized under mildly acidic conditions than the FeNCs (Figure S10). These results suggest the AFeNPs to be the preferable ferrous ion carrier (Figure S11), as they will be present as Fe^0 in neutral normal tissues (pH ≈ 7.4), but be ionized rapidly for ferrous ion release once located in acidic cancer tissue (extracellular environment, pH ≈ 6.5). This release will be significantly accelerated after cell endocytosis (in endosomes or lysosomes, pH ≈ 5.4).[16]

The above characterizations demonstrate the remarkable advantages of AFeNPs for on-demand ferrous ion release, aside from their favorable dispersity and T_1-weighted MRI signals, which enables endogenous chemodynamic therapy without the need for any external stimuli. The potential of the AFeNPs to act as a trigger for the generation of hydroxyl radicals was first investigated. Methylene blue (MB) decolorization (Figure S12) and electron spin resonance (ESR) spectroscopy (Figure 4a) experiments confirmed that AFeNPs, acidic conditions, and hydrogen peroxide are the three necessary factors for producing ·OH. The increased ESR signal intensity at lower pH values suggests the generation of a great number of ·OH radicals, which may be attributed to enhanced ferrous ion release and the acceleration of the Fenton reaction in a more acidic environment.[17]

Encouraged by the suitability of the AFeNPs for selective ·OH generation and their good biocompatibility (Figure S13), we evaluated their in vitro anticancer effect. An acidic culture medium of pH 6.5 to which a safe dose of H_2O_2 had been added was employed to simulate the moderately acidic and H_2O_2 overproducing tumor microenvironment, and was shown to have negligible influence on the viability of MCF-7 human breast adenocarcinoma cells (Figure S14). As shown in Figure 4b, the observation that a low concentration of H_2O_2 promotes cell proliferation may result from enhanced mitogenic action of growth factor/cytokine in cell signaling.[18] In the presence of AFeNPs and H_2O_2, there is significant AFeNP dose dependent cytotoxicity at pH 6.5, whereas the cell viability decreased only slightly (still almost 100%) at pH 7.4. At pH 6.5, the reduction in cell viability after 24 hours of incubation amounted to more than 40 and 60% at AFeNP concentrations of 100 and 200 ppm, respectively. When 2′,7′-dichlorofluorescein diacetate (DCFH-DA) was added as a ROS probe, these cells displayed fluorescence within 15 min after AFeNPs and H_2O_2 had been simultaneously added to the acidic DMEM solution, and the green fluorescence was further enhanced by continuous incubation for one hour (Figure 4c). Various morphological characteristics of

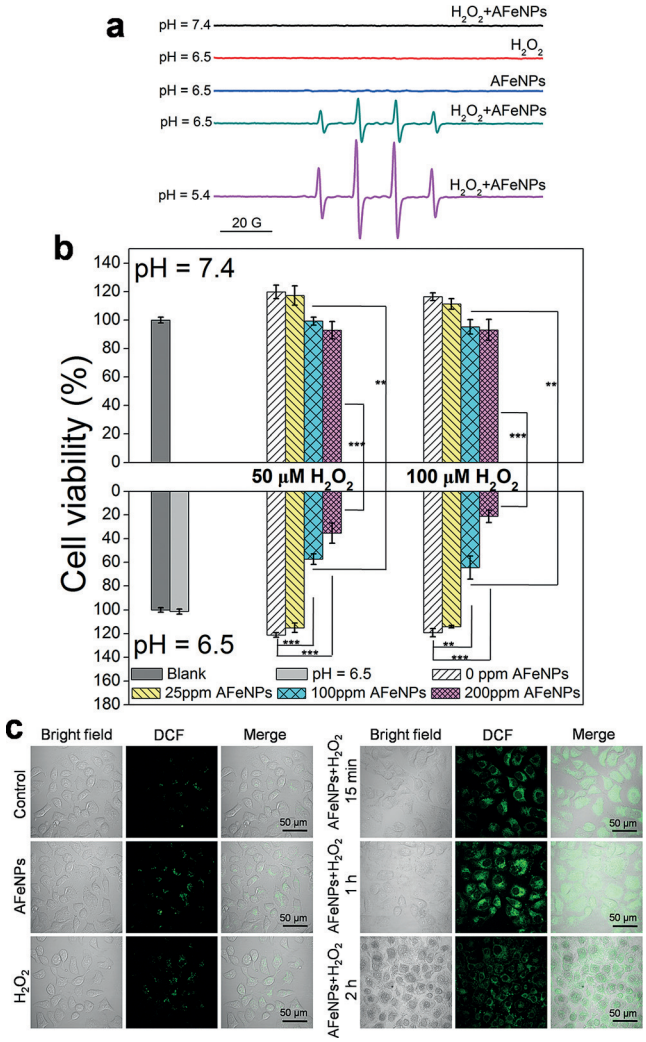

Figure 4. a) ESR spectra of different reaction systems with DMPO as the spin trap. b) Growth inhibitory effects of the AFeNPs on MCF-7 cells at pH 7.4 and 6.5 at various H_2O_2 concentrations ($n = 6$, mean ± s.d., $^{**}P < 0.01$, and $^{***}P < 0.001$). c) Confocal images of DCFH-DA stained MCF-7 cells treated with AFeNPs only, H_2O_2 only, and both at pH 6.5.

ROS-induced cell apoptosis, such as cell-membrane damage and nuclei shrinkage, were observed two hours after co-incubation, which were similar to the well-defined cellular morphology changes observed after the administration of PDT.[19] Furthermore, magnetic targeting and the retention of the AFeNPs lead to selective anticancer effects (Figure S15). These results confirm that the AFeNPs, hydrogen peroxide, and acidic conditions act synergistically to kill cells, implying that AFeNP-induced specific CDT of tumors, which are inherently mildly acidic and over-produce hydrogen peroxide, should be possible.

Before in vivo administration, these AFeNPs were evaluated to be of excellent biosafety (Figures S16 and S17). To further confirm that the nanoparticles are enriched in the tumor by MR imaging in vivo, a bilateral 4T1 tumor-xenografted mouse was used, with a button magnet temporarily fixed on the right tumor for magnetic targeting (Fig-

ure S18). One hour after the intravenous (i.v.) injection of AFeNPs, a significant increase of 38% in the T_1 MRI signal intensity could be observed in the right tumor, to which the magnet had been attached (Figure 5a, Figure S19), indicating that efficient magnetic targeting and retention had been achieved in vivo, providing a good basis for CDT.

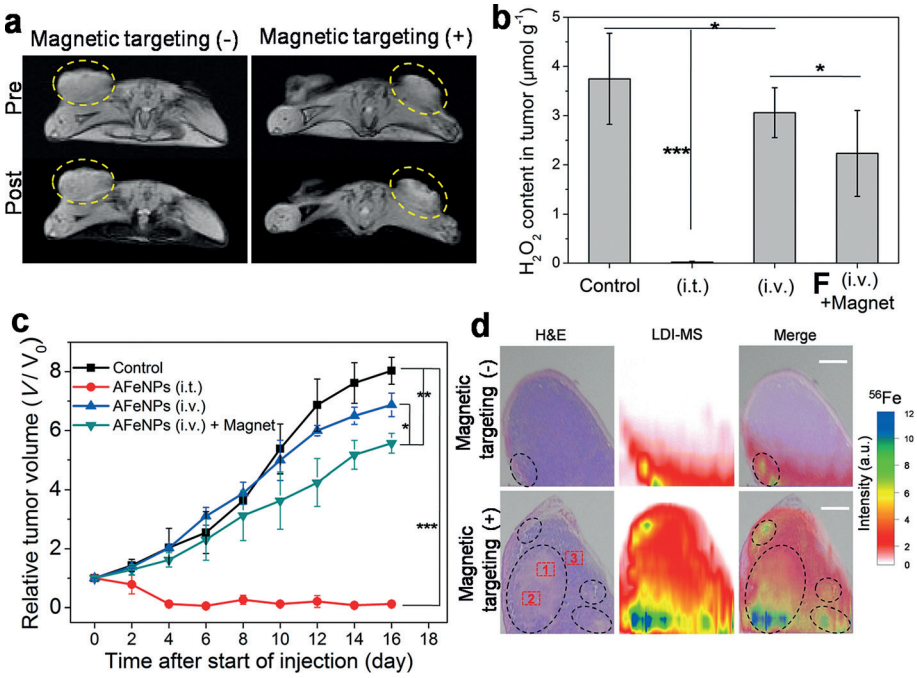

Figure 5. a) Coronal T_1-weighted MR images of 4T1 tumor-bearing mice before and one hour after i.v. injection of AFeNPs with (right, +) or without (left, −) magnetic targeting. b) Change in the H_2O_2 concentration in the tumor after different treatment procedures, namely intratumoral AFeNP injection ((i.t.)) and intravenous AFeNP injection without ((i.v.)) and with magnetic targeting ((i.v.)+magnet; $n=3$, mean ± s.d., $*P<0.05$, and $***P<0.001$). c) Change in the relative tumor volume after different treatments ($n=5$, mean ± s.d., $*P<0.05$, $**P<0.01$, and $***P<0.001$). d) H&E staining images, LDI-MS ^{56}Fe mapping, and merged images of tumor tissues after i.v. AFeNP injection with or without magnetic targeting. The circles highlight the isolated pockets.

We have shown above that the CDT mode of action of the AFeNPs is based on the rapid release of ferrous ions under acidic conditions; they promote the disproportionation of H_2O_2, which produces reactive ·OH species. Therefore, a sharp decrease in intratumoral H_2O_2 concentration is a key indicator for therapeutic efficacy, which is mainly dependent on the AFeNP concentration in the tumor and their ionization efficiency. Compared with the control group, a drastic decrease in intratumoral H_2O_2 concentration could be observed in the group that had been subjected to intratumoral (i.t.) AFeNP injection (Figure 5b), which led to a complete inhibition of tumor growth within 16 days (Figure 5c, Figure S20). Such a superior anticancer effect implemented by i.t. injection implies efficient iron ionization and H_2O_2 disproportionation, leading to the generation of ·OH species that induce a localized, intratumoral Fenton reaction.

Furthermore, Fe mapping by laser desorption/ionization mass spectrometry (LDI-MS; Figure 5d) revealed that magnetic targeting led to more significant AFeNP enrichment, which led to a greater decrease in intratumoral H_2O_2 concentration and significantly higher tumor growth inhibition with an inhibition ratio of 27% after 16 days (Figures 5c and S21). In the control group that had not been subjected to magnetic targeting, tumor growth inhibition was significantly less effective and only achieved through the enhanced permeability and retention (EPR) effect. The well-defined isolated pockets in the damaged tumor tissue corroborate the CDT anticancer mechanism of the AFeNPs and their promising potential for selective cancer therapy (Figures S22 and S23). Nevertheless, it should also be noted that the i.v. injection group displayed much lower anticancer efficacy than the i.t. injection group even under magnetic targeting. External magnetic targeting, however, is not satisfactory; better results may be achieved by seeking for other active targeting mechanisms, such as ligand–receptor interactions.

In conclusion, we have presented a hubble-bubble approach for the synthesis of amorphous iron nanoparticles, which show remarkable advantages over the corresponding nanocrystalline particles and can be used as theranostic agents benefiting from their glassy nature. In theory, for the extensively studied inorganic theranostic agents facing clinical applications, amorphization may provide a versatile strategy to improve their biodegradability and magnetism-related properties (MRI and magnetic targeting) owing to the disordered atomic arrangement. To the best of our knowledge, this is the first study that employs a Fenton reaction that is induced by the specific properties of the tumor microenvironment, which includes the ionization of AFeNPs for on-demand ferrous ion release and subsequent H_2O_2 disproportionation for efficient ·OH generation. Whereas we still aim to improve their tumor-targeting properties by further surface modifications, we believe that the present study may open the way for further explorations and applications of amorphous metal nanoparticles in various fields, such as bioimaging, tumor therapy, and catalysis.

Acknowledgements

This work was financially supported by the National Natural Science Foundation of China (51372260, 51132009) and the Natural Science Foundation of Shanghai (15ZR1407700). We thank Jiafu Chen (Hefei National Laboratory for Physical

Sciences at the Microscale, University of Science and Technology of China) for assistance with the ESR measurements. We acknowledge Linlin Zhang, Jingwei Feng, Yanyan Liu, Qingfeng Xiao, and Huaiyong Xing (Shanghai Institute of Ceramics, Chinese Academy of Sciences) for useful discussions.

Keywords: antitumor agents · cancer · Fenton reaction · iron nanoparticles · magnetic resonance imaging

How to cite: *Angew. Chem. Int. Ed.* **2016**, *55*, 2101–2106
Angew. Chem. **2016**, *128*, 2141–2146

[1] W. Klement, R. Willens, *Nature* **1960**, *187*, 869–870.
[2] a) Y. H. Liu, G. Wang, R. J. Wang, D. Q. Zhao, M. X. Pan, W. H. Wang, *Science* **2007**, *315*, 1385–1388; b) M. D. Demetriou, M. E. Launey, G. Garrett, J. P. Schramm, D. C. Hofmann, W. L. Johnson, R. O. Ritchie, *Nat. Mater.* **2011**, *10*, 123–128; c) M. Chen, *NPG Asia Mater.* **2011**, *3*, 82–90.
[3] J. Q. Wang, Y. H. Liu, M. W. Chen, G. Q. Xie, D. V. Louzguine-Luzgin, A. Inoue, J. H. Perepezko, *Adv. Funct. Mater.* **2012**, *22*, 2567–2570.
[4] J. Q. Wang, N. Chen, P. Liu, Z. Wang, D. V. Louzguine-Luzgin, M. W. Chen, J. H. Perepezko, *Acta Mater.* **2014**, *62*, 30–36.
[5] a) F. Muhammad, M. Guo, W. Qi, F. Sun, A. Wang, Y. Guo, G. Zhu, *J. Am. Chem. Soc.* **2011**, *133*, 8778–8781; b) R. van Sluis, Z. M. Bhujwalla, N. Raghunand, P. Ballesteros, J. Alvarez, S. Cerdán, J.-P. Galons, R. J. Gillies, *Magn. Reson. Med.* **1999**, *41*, 743–750; c) V. Estrella, T. Chen, M. Lloyd, J. Wojtkowiak, H. H. Cornnell, A. Ibrahim-Hashim, K. Bailey, Y. Balagurunathan, J. M. Rothberg, B. F. Sloane, *Cancer Res.* **2013**, *73*, 1524–1535; d) M. Zan, J. Li, S. Luo, Z. Ge, *Chem. Commun.* **2014**, *50*, 7824–7827; e) S. Mura, J. Nicolas, P. Couvreur, *Nat. Mater.* **2013**, *12*, 991–1003.
[6] M. López-Lázaro, *Cancer Lett.* **2007**, *252*, 1–8.
[7] a) C. D. G. Lux, S. Joshi-Barr, T. Nguyen, E. Mahmoud, E. Schopf, N. Fomina, A. Almutairi, *J. Am. Chem. Soc.* **2012**, *134*, 15758–15764; b) Y. Zhang, Q. Yin, L. Yin, L. Ma, L. Tang, J. Cheng, *Angew. Chem. Int. Ed.* **2013**, *52*, 6435–6439; *Angew. Chem.* **2013**, *125*, 6563–6567; c) F. Muhammad, A. Wang, L. Miao, P. Wang, Q. Li, J. Liu, J. Du, G. Zhu, *Langmuir* **2014**, *30*, 514–521.
[8] H. Chen, J. Tian, W. He, Z. Guo, *J. Am. Chem. Soc.* **2015**, *137*, 1539–1547.
[9] H. Fenton, *J. Chem. Soc. Trans.* **1894**, *65*, 899–910.
[10] W. A. Wlassoff, C. D. Albright, M. S. Sivashinski, A. Ivanova, J. G. Appelbaum, R. I. Salganik, *J. Pharm. Pharmacol.* **2007**, *59*, 1549–1553.
[11] D. Lee, S. Khaja, J. C. Velasquez-Castano, M. Dasari, C. Sun, J. Petros, W. R. Taylor, N. Murthy, *Nat. Mater.* **2007**, *6*, 765–769.
[12] M. E. McHenry, M. A. Willard, D. E. Laughlin, *Prog. Mater. Sci.* **1999**, *44*, 291–433.
[13] M. W. Grinstaff, M. B. Salamon, K. S. Suslick, *Phys. Rev. B* **1993**, *48*, 269.
[14] a) G. Wang, X. Zhang, A. Skallberg, Y. Liu, Z. Hu, X. Mei, K. Uvdal, *Nanoscale* **2014**, *6*, 2953; b) Y.-w. Jun, Y.-M. Huh, J.-s. Choi, J.-H. Lee, H.-T. Song, S. J. Kim, S. Yoon, K.-S. Kim, J.-S. Shin, J.-S. Suh, J. Cheon, *J. Am. Chem. Soc.* **2005**, *127*, 5732–5733; c) Y. W. Jun, J. H. Lee, J. Cheon, *Angew. Chem. Int. Ed.* **2008**, *47*, 5122–5135; *Angew. Chem.* **2008**, *120*, 5200–5213; d) B. H. Kim, N. Lee, H. Kim, K. An, Y. I. Park, Y. Choi, K. Shin, Y. Lee, S. G. Kwon, H. B. Na, J. G. Park, T. Y. Ahn, Y. W. Kim, W. K. Moon, S. H. Choi, T. Hyeon, *J. Am. Chem. Soc.* **2011**, *133*, 12624–12631.
[15] a) L. Yang, Z. Zhou, H. Liu, C. Wu, H. Zhang, G. Huang, H. Ai, J. Gao, *Nanoscale* **2015**, *7*, 6843–6850; b) D. Yoo, J.-H. Lee, T. H. Shin, J. Cheon, *Acc. Chem. Res.* **2011**, *44*, 863–874.
[16] D. Schmaljohann, *Adv. Drug Delivery Rev.* **2006**, *58*, 1655–1670.
[17] Y. S. Jung, W. T. Lim, J. Y. Park, Y. H. Kim, *Environ. Technol.* **2009**, *30*, 183–190.
[18] a) Q. Pan, W. Y. Qiu, Y. N. Huo, Y. F. Yao, M. F. Lou, *Invest. Ophthalmol. Visual Sci.* **2011**, *52*, 1723–1734; b) D. B. Peden, L. Dailey, W. DeGraff, J. B. Mitchell, J. Lee, M. A. Kaliner, R. J. Hohman, *Am. J. Physiol. Lung Cell Physiol.* **1994**, *267*, 85–93.
[19] a) N. M. Idris, M. K. Gnanasammandhan, J. Zhang, P. C. Ho, R. Mahendran, Y. Zhang, *Nat. Med.* **2012**, *18*, 1580–1585; b) J. Ge, M. Lan, B. Zhou, W. Liu, L. Guo, H. Wang, Q. Jia, G. Niu, X. Huang, H. Zhou, X. Meng, P. Wang, C. S. Lee, W. Zhang, X. Han, *Nat. Commun.* **2014**, *5*, 4596; c) J. Tian, L. Ding, H. J. Xu, Z. Shen, H. Ju, L. Jia, L. Bao, J. S. Yu, *J. Am. Chem. Soc.* **2013**, *135*, 18850–18858.

Received: October 28, 2015
Published online: January 6, 2016

